RAA 2020 Vol. **20** No. **5**, 77(12pp) doi: 10.1088/1674–4527/20/5/77

http://www.raa-journal.org *http://iopscience.iop.org/raa*

***R**esearch in*
***A**stronomy and*
***A**strophysics*

Pilot HI survey of Planck Galactic Cold Clumps with FAST

Ning-Yu Tang (汤宁宇)[1,2], Pei Zuo (左沛)[3], Di Li (李荫)[1,2,4], Lei Qian[1,2], Tie Liu[5,6], Yue-Fang Wu[7], Marko Krčo[1,2], Meng-Ting Liu[1,2], You-Ling Yue[1,2], Yan Zhu[1,2], Hong-Fei Liu[1,2], Dong-Jun Yu[1,2], Jing-Hai Sun[1,2], Peng Jiang[1,2], Gao-Feng Pan[1,2], Hui Li[1,2], Heng-Qian Gan[1,2], Rui Yao[1,2], Shu Liu[1,2] and FAST Collaboration[1]

[1] National Astronomical Observatories, Chinese Academy of Sciences, Beijing 100101, China; *nytang@nao.cas.cn, dili@nao.cas.cn, lqian@nao.cas.cn*
[2] CAS Key Laboratory of FAST, National Astronomical Observatories, Chinese Academy of Sciences, Beijing 100101, China
[3] Kavli Institute for Astronomy and Astrophysics, Peking University, Beijing 100871, China
[4] School of Astronomy and Space Science, University of Chinese Academy of Sciences, Beijing 100049, China
[5] Shanghai Astronomical Observatory, Chinese Academy of Sciences, Shanghai 200030, China
[6] East Asian Observatory, 660 North A'ohoku Place, Hilo, HI 96720, USA
[7] Department of Astronomy, School of Physics, Peking University, Beijing 100871, China

Received 2019 April 1; accepted 2019 September 11

Abstract We present a pilot HI survey of 17 Planck Galactic Cold Clumps (PGCCs) with the Five-hundred-meter Aperture Spherical radio Telescope (FAST). HI Narrow Self-Absorption (HINSA) is an effective method to detect cold HI being mixed with molecular hydrogen H_2 and improves our understanding of the atomic to molecular transition in the interstellar medium. HINSA was found in 58% PGCCs that we observed. The column density of HINSA was found to have an intermediate correlation with that of ^{13}CO, following $\log(N(\mathrm{HINSA})) = (0.52 \pm 0.26)\log(N_{^{13}\mathrm{CO}}) + (10 \pm 4.1)$. HI abundance relative to total hydrogen [HI]/[H] has an average value of 4.4×10^{-3}, which is about 2.8 times of the average value of previous HINSA surveys toward molecular clouds. For clouds with total column density $N_{\mathrm{H}} > 5 \times 10^{20}$ cm^{-2}, an inverse correlation between HINSA abundance and total hydrogen column density is found, confirming the depletion of cold HI gas during molecular gas formation in more massive clouds. Non-thermal line width of ^{13}CO is about $0 - 0.5$ km s^{-1} larger than that of HINSA. One possible explanation of narrower non-thermal width of HINSA is that HINSA region is smaller than that of ^{13}CO. Based on an analytic model of H_2 formation and H_2 dissociation by cosmic ray, we found the cloud ages to be within $10^{6.7} - 10^{7.0}$ yr for five sources.

Key words: ISM: clouds — ISM: evolution — ISM: molecules

1 INTRODUCTION

Cold molecular cores/clumps are the cradles of star formation. Statistical properties of prestellar cores/clumps are beneficial for understanding the general evolution progress of star formation. The Planck Catalogue of Galactic cold clumps (PGCCs) released by Planck satellite (Planck Collaboration et al. 2016) contains 13 188 sources with dust temperature ranging from 5.8 to 20 K. These cold clumps, identified based on the 5′ beam of Planck, contain low-mass cores to large molecular clouds, providing us a chance of investigating star formation in various scales, from 0.1 to tens of pc.

Spectral observations toward PGCCs provide extra kinematic and chemical properties compared to multi-band continuum observations. Molecular line surveys have been taken in CO(1-0) (Wu et al. 2012; Liu et al. 2012, 2016, 2018), C_2H ($N = 1 - 0$) and N_2H^+ ($J = 1 - 0$) (Liu et al. 2019), HCO^+ and HCN ($J = 1 - 0$) (Yuan et al. 2016). These molecular transitions are collisionally excited with critical density $n_{\mathrm{crit}} \gtrsim 10^3$ cm^{-3}, making them tracers of dense gas. With multiple tracers, the age of a cloud can

be modeled through chemical reaction networks to reproduce the observed line ratio, e.g., $[C_2H]/[N_2H^+]$ (Pan et al. 2017; Liu et al. 2019). Such estimate, however, is hardly quantitative calculation and model dependent, due to the complexities of reaction networks and incomplete knowledge of key parameters, such as densities.

HI could also be a tracer of cloud age. When a cloud cools and evolves, the abundance of HI in the cloud decreases with time. Cosmic ray dissociation maintains a small content of HI even in the central, dense region of molecular clouds, where HI is shielded from being dissociated by UV photons and cools through collision with H_2 (Solomon & Werner 1971; Goldsmith & Li 2005). The cold HI appears as absorption against its bright HI background and correlates with molecular emission. It is called HI Narrow Self-Absorption (HINSA), and has been widely detected toward dark clouds in the Taurus/Perseus region and nearby molecular clouds (Li & Goldsmith 2003) and molecular clouds (Krčo & Goldsmith 2010). HINSA is a special case of HI Self-Absorption (HISA), which is common and has been introduced as an effective tool to study Galactic HI distribution (e.g., Gibson et al. 2000; Dickey et al. 2003; Kavars et al. 2003). HISA usually arises in cold neutral medium (CNM) from different mechanisms, e.g., temperature fluctuations, thus may not match with molecular emission. For the case of HINSA, it is closely associated with molecular clouds in terms of sky position, velocity, and non-thermal line width. With HINSA analysis, a "ring" of enhanced HI abundance was clearly seen toward dark cloud B227 (Zuo et al. 2018).

With an instantaneous effective area of 300 m diameter, the Five-hundred-meter Aperture Spherical radio Telescope (FAST, Nan et al. 2011) located in the southwest of China is the most sensitive radio telescope in HI band. FAST began its commissioning after 2016 Sep 25. Its commissioning progress was reviewed in Jiang et al. (2019). The 19 beam receiver was installed on FAST in mid May of 2018. Spectral back-end for the 19 beam receiver was installed in late July, 2018.

In this paper, we introduce pilot spectral observations with 19 beam receiver of FAST. The paper is structured as follows: Observation information is described in Section 2. Analysis of deriving physical parameters is shown in Section 3. The results and discussion are presented in Section 4. We summarize our conclusion in Section 5.

2 OBSERVATIONS AND DATA ARCHIVE

2.1 Observations of HI

We selected our sources from the catalogue of Wu et al. (2012) and its follow-up survey projects, in which more than 674 PGCCs were observed in $J = 1 - 0$ transition of CO and its isotopes. Two criteria were applied: (1) position of the source is within FAST sky coverage but is out of sky coverage of Arecibo 305 m telescope; (2) strong CO emission is detected toward the source. Position distribution of observed 17 PGCCs is shown in Figure 1.

The FAST observations were conducted between 2018 December 16 and 2019 January 2. We observed the HI 1420.4058 MHz transition with the central beam of the 19-beam receiver on FAST, which corresponds to a beam width (Full Width at Half Maximum; FWHM) of 2.9 arcmin. The pointing error is $\sim$0.15 arcmin at 1420 MHz (Jiang et al. 2019).

Single pointing observations of PGCCs were taken with the narrow mode of spectral back-end. This mode has 65 536 channels in 31.25 MHz bandwidth, resulting in velocity resolution of 0.1 km s^{-1} at 1.420 GHz. Each source was integrated for 10 minutes with a sampling rate of 1.0066 s. For intensity calibration, noise signal with amplitude of $\sim$ 11 K was injected under a period of 2.0132 s, which is synchronized with sampling rate.

After intensity calibration, spectral baseline was removed by applying a linear fitting of line-free range within [$-$300,300] km s^{-1}. During observations, system temperature was around 18 K. Reduced root mean square (rms) of the final spectrum is $\sim$35 mK, which is consistent with theoretical sensitivity calculation. FAST's current setup does not include a local oscillator (LO), and therefore neither Doppler tracking nor frequency switching are available.

In order to test the validity of our data reduction, the PGCC source G089.29+03.99 located within the sky coverage of Arecibo telescope was observed. The observed spectrum with FAST is expressed in antenna temperature ($T_{\rm A}$) while the data of GALFA-HI (Peek et al. 2011, 2018) is expressed in brightness temperature ($T_{\rm B}$). We define a ratio R to convert measured $T_{\rm A}$ to $T_{\rm B}$, $R = T_{\rm B}/T_{\rm A}$. A value of $R = 1.15$ is used for comparing observation results of G089.29+03.99. As shown in Figure 2, we have consistent spectrum for FAST and Arecibo.

At HI band, telescope efficiency of FAST is almost a constant value of $\sim$0.6 when zenith angle (ZA) is less than 26.4° and decreases linearly when ZA is greater than 26.4° (Jiang et al. 2019). This implies an R value of 1.67 within ZA$< 26.4°$. This value is larger than required conversion value of 1.15 between FAST and Arecibo toward G089.29+03.99. Three main effects may contribute to this difference.

1. The GALFA-HI map was not sampled at the center position precisely of the PGCC source G098.29+03.99, while we pointed directly at the source.

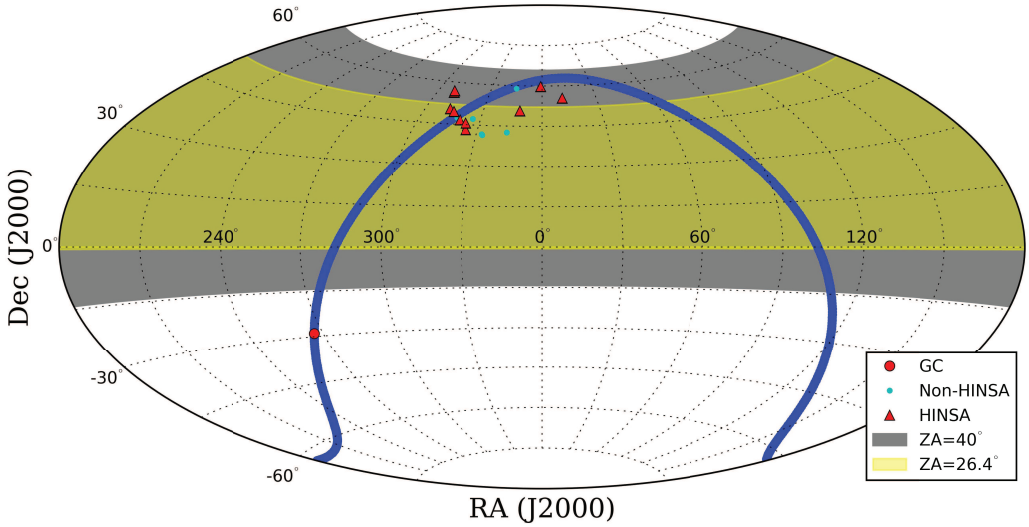

Fig. 1 Spatial distribution of observed 17 PGCCs. Sources with and without HINSA detection are labeled with cyan circles and red triangles. Sky coverage of FAST within zenith angle (ZA) of 26.4 and 40 degree is shown with *yellow* and *grey color*. The Galactic plane and Galactic center (GC) are shown with a *blue solid line* and a *red circle*, respectively.

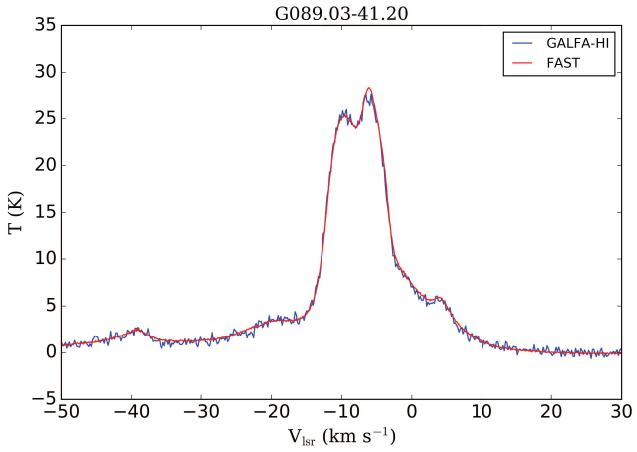

Fig. 2 HI spectra for PGCC source G089.03–41.2. *Blue* and *red color* represents data from GALFA-HI and FAST, respectively. The amplitude of FAST data has been multiplied by a factor of 1.15.

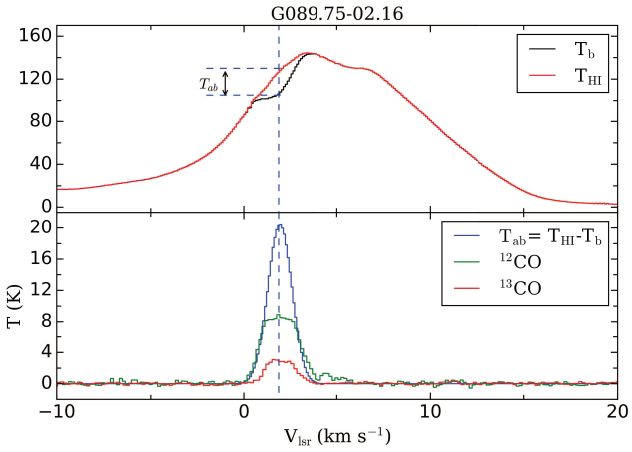

Fig. 3 An example of HINSA fitting toward G089.75–02.16. *Top panel*: *black* and *red solid lines* are the observed HI and the recovered HI background spectrum $T_{\rm HI}$, respectively. *Bottom panel*: The profile of absorption temperature $T_{\rm ab}$ (*blue*), ^{12}CO (*green*) and ^{13}CO spectrum (*red*).

2. The flux for the GALFA-HI map was bootstrapped using the Leiden/Argentine/Bonn (LAB) survey (Kalberla et al. 2005). This means that while on a large scale the flux of the map is very accurate, there may be small-scale fluctuations.
3. The GALFA map was partially corrected for stray radiation, while we did not.

We applied $R = 1.67$ and corrected its dependence of ZA to derive $T_{\rm B}$ from $T_{\rm A}$.

2.2 CO and Dust Archive Data

The ^{12}CO(1–0) and ^{13}CO(1–0) data were obtained under single pointing mode for investigating dynamic evolution of PGCCs with PMO 13.7m and TRAO-14m telescopes (Wu et al. 2012; Liu et al. 2016). Angular resolution of both PMO 13.7m and TRAO-14m is ∼1 arcmin (FWHM) at 115 GHz. The back-end of PMO 13.7m provides bandwidth of 1 GHz and frequency resolution of 61 kHz (0.16 km s^{-1} for ^{12}CO and 0.17 km s^{-1} for ^{13}CO). The back-end of TRAO-14m provides bandwidth of 125 MHz and frequency resolution of 15 kHz. This frequency resolution leads to velocity resolution of 0.04 km s^{-1} at 115.271 GHz. The spectral resolution of TRAO-14m were smoothed to that of PMO 13.7m.

The dust temperature and dust reddening toward each source were derived from Planck Collaboration et al.

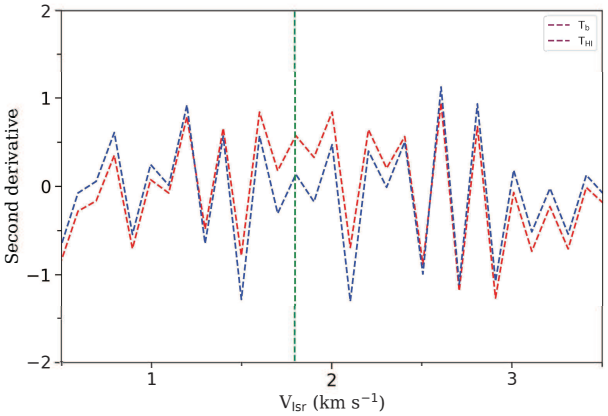

Fig. 4 Second derivatives of $T_{\rm HI}$ and $T_{\rm b}$ profile for G089.75–02.16. The velocity range is [0.5, 3.5] km s^{-1}. *The vertical dashed line* represents the central velocity of the HINSA component.

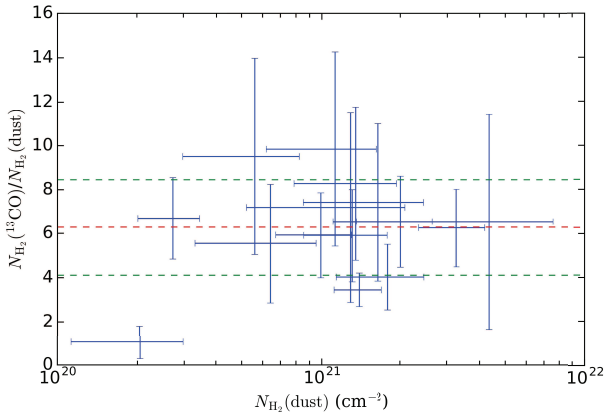

Fig. 5 The $N_{\rm H_2}(^{13}{\rm CO})/N_{\rm H_2}({\rm dust})$ ratio as a function of $N_{\rm H_2}({\rm dust})$. $N_{\rm H_2}(^{13}{\rm CO})$ and $N_{\rm H_2}({\rm dust})$ are estimated molecular hydrogen from $N(^{13}{\rm CO})$ with converstion factor of 1.67×10^{-6} and dust (Planck Collaboration et al. 2016), respectively. *Red* and *green dashed lines* represent averaged value and 1σ deviation, respectively.

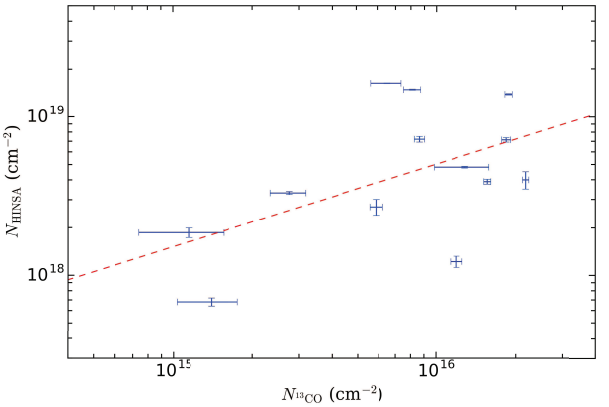

Fig. 6 Correlation between column density of HINSA and ^{13}CO. The *red dashed line* represents linear fitting of the data.

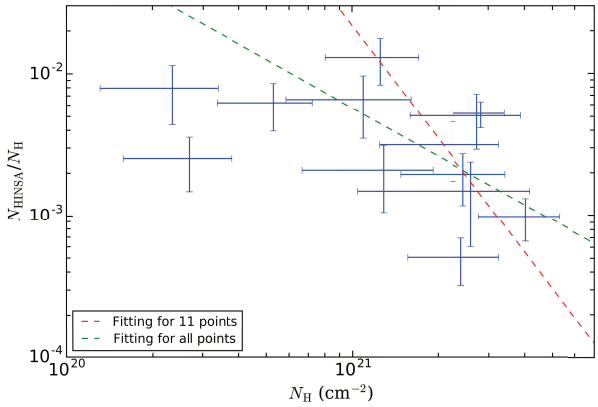

Fig. 7 The relation between HINSA abundance $N_{\rm HINSA}/N_{\rm H}$ compared to total hydrogen $N_{\rm H}$. The *red* and *green dashed lines* represent fitting for the right 11 data points and all 13 data points.

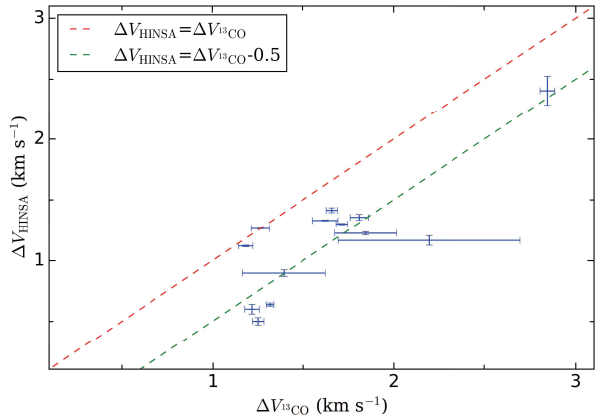

Fig. 8 Non-thermal width of HINSA and ^{13}CO.

(2016), in which the data were smoothed into FWHM of 5 arcmin.

3 ANALYSIS

We start analysis by identifying molecular components in velocity based on multiple gaussian fitting of molecular spectrum. There are two factors: ^{12}CO profile may be affected by self-absorption due to its large optical depth, making it difficult to distinguish component numbers; C^{18}O has a relatively low abundance compared to ^{12}CO. Its emission is weak and may be 'missed' under our observational sensitivity. Considering these factors, we identify velocity components with ^{13}CO spectral data, whose emission is relatively optically thinner than ^{12}CO and strong enough to be detected. A total of 23 components are identified toward 17 PGCCs. Each component is fitted with a Gaussian function.

Next, we check if there exists a corresponding HI absorption feature toward each ^{13}CO emission component. HI fluctuation is common in HI spectra. It may arise from either kinematic effect of two HI clouds in different veloc-

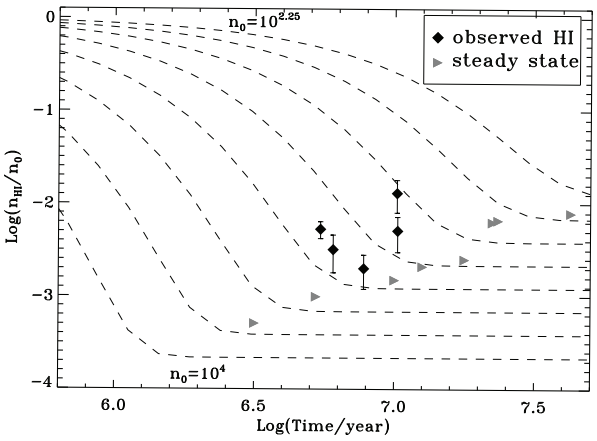

Fig. 9 Time dependence of HI abundance for various proton density (in cm^{-3}). The *dashed lines* represent different logarithmic densities with index interval of 0.25. Five sources are plotted with *black diamonds*. The cloud age of remaining eight sources is calculated with measured HI abundance and the assumption of steady state. They are shown with *grey triangles*.

ity or absorption of cold HI cloud against brighter HI background. A feature of HI fluctuation is identified as HINSA only when there is corresponding ^{12}CO or ^{13}CO emission. This method of identifying HINSA through single pointing spectrum could not absolutely exclude the coincidence between HI fluctuation from kinematic effect and ^{13}CO emission. As discussed in Gibson et al. (2000), geometry inspection of HI mapping would improve this situation.

For these identified HINSA components, we calculated excitation temperature and column density of atomic and molecular content. They are shown as follows.

3.1 CO Excitation

For all observed PGCCs components, temperature ratio between ^{12}CO and ^{13}CO emission is around 2. This value is much smaller than Galactic [^{12}C/^{13}C] ratio ($\sim$ 60; Lucas & Liszt 1998) in interstellar medium (ISM), leading to a reasonable assumption that ^{12}CO is optically thick, $\tau_{12} \geq 1$. Assuming a filling factor of 1, the excitation temperature of ^{12}CO equals brightness temperature of ^{12}CO.

The excitation temperature of ^{13}CO, $T_{\rm ex}^{\rm ^{13}CO}$ is assumed to be same of $T_{\rm ex}^{\rm ^{12}CO}$. The optical depth of ^{13}CO, τ_{13} is given by

$$\tau_{13} = -\ln(1 - \frac{T_{\rm b}^{13}}{T_{\rm b}^{12}}) \,, \quad (1)$$

under the assumption of $\tau_{12} \geq 1$.

The column density of ^{13}CO is derived through the following equation (Li 2002; Qian et al. 2012):

$$N_{\rm tot}^{\rm ^{13}CO} = 3.70 \times 10^{14} \times \int \frac{T_{\rm b}^{13}}{K} \frac{dv}{\rm km\ s^{-1}} f_u f_{\tau_{13}} f_{\rm b} \frac{1}{f_{\rm beam}}\ {\rm cm^{-2}}, \quad (2)$$

in which $T_{\rm b}^{13}$ is brightness temperature of ^{13}CO, $f_{\tau_{13}}$ is the optical depth of ^{13}CO, $f_{\tau_{13}} = \int \tau_{13} dv / \int (1 - e^{-\tau_{13}}) dv$. The uncertainty of $N_{\rm tot}^{\rm ^{13}CO}$ was calculated by uncertainty propagation of spectral rms of ^{12}CO and ^{13}CO data.

The above analysis of ^{13}CO is derived under the assumption of local thermal equilibrium (LTE). Application of non-LTE analysis leads to a consistent result with that of LTE for PGCC (Liu et al. 2016).

3.2 Physical Parameters of HINSA

Li & Goldsmith (2003) proposed a three-component model of HINSA, which consists of warm HI background and foreground gas with a central cold HI cloud along line of sight. In this model, optical depth of background and foreground HI gas are τ_b and τ_f, respectively. The factor p is defined as $p = \tau_f/(\tau_f + \tau_b)$. Kinematic distance of each PGCC component was derived through Galactic rotation curve (Brand & Blitz 1993). We combine kinematic distance and Galactic HI surface density distribution (Nakanishi & Sofue 2003) to estimate p along sightline of the PGCC. This is different from the formula adopted in Li & Goldsmith (2003), which is reasonable for cloud with high Galactic latitude but would be invalid for cloud in the Galactic plane. Details of this calculation could be found in section 4.2 of Tang et al. (2016). $T_{\rm b}(\upsilon)$ and $T_{\rm HI}(\upsilon)$ represent observed HI brightness temperature spectrum and brightness temperature spectrum when central cold HI cloud is absent, respectively. Absorption temperature, $T_{\rm ab}(\upsilon) = T_{\rm HI}(\upsilon) - T_{\rm b}(\upsilon)$ could be described with (Li & Goldsmith 2003):

$$T_{\rm ab}(\upsilon) = [pT_{\rm HI}(\upsilon) + (T_{\rm c} - T_{\rm x})(1 - \tau_f)](1 - e^{-\tau}), \quad (3)$$

where $T_{\rm c}$ is continuum temperature including cosmic microwave background (CMB, 2.73 K), Galactic synchrotron radiation ($\sim$0.7 K), and continuous emission from other radiation mechanisms. The value of $T_{\rm c}$ is derived by the equation $T_{\rm c} = 2.7 + T_{\rm c408}(\nu_{\rm HI}/408\ {\rm MHz})^{-2.8}$, in which T_{c408} is continuum temperature around 408 MHz (Haslam et al. 1982), and $\nu_{\rm HI}$ is frequency of HI emission. Derived value of $T_{\rm c}$ toward our targets ranges from 3.8 to 5.6 K. $T_{\rm x}$ is the excitation temperature of HINSA component, and depends on kinetic temperature $T_{\rm k}$ and effective temperature of radiation field. The gas of observed PGCCs are in molecular phase, resulting a reasonable assumption that $T_{\rm x} = T_{\rm k}$. The value of p is around 0.9. We follow Li & Goldsmith (2003), the value of τ_f is assumed as 0.1, which implies a total optical depth of unity along Galactic sightline. This assumption would not significantly affect the result. The optical depth of HINSA, τ is an unknown parameter to be solved. Assuming a Gaussian broadening, τ is

described in the formula of $\tau = \tau_0 e^{-\frac{(v-v_0)^2}{2\sigma^2}}$, in which τ_0 is peak optical depth at central velocity.

$T_{\rm HI}$ is recovered HI spectrum without absorption from the central cold cloud. There are many methods to derive $T_{\rm HI}$, for instance, averaging nearby spectra without this absorption cloud (e.g., Gibson et al. 2000) or fitting observed profile with polynomial (e.g., Li & Goldsmith 2003). Considering complexity of HI emission around the Galactic plane, the method of observing off positions or fitting with polynomial may introduce significant uncertainty. The method of polynomial fitting depends on the choice of polynomial index.

HINSA and molecular hydrogen are believed to mix well inside the cloud. Total velocity broadening of each transition, $\sigma_{\rm tot} = \sqrt{\sigma_{\rm th}^2 + \sigma_{\rm nt}^2}$, in which $\sigma_{\rm th}$ and $\sigma_{\rm nt}$ represent thermal broadening due to collision and non-thermal broadening including turbulence, magnetic field and other effects. Krčo et al. (2008) introduced a new method to derive $T_{\rm HI}$ by utilizing physical information (central velocity, non-thermal linewidth and kinematic temperature) derived from CO data to constrain fitting of HINSA profile. We introduce this method for analysis in this paper. For each HINSA component, four parameters of HINSA are fitted with the following considerations (Krčo & Goldsmith 2010):

1. Central velocity. A maximum deviation of 10% linewidth from central velocities of ^{13}CO is allowed.
2. Non-thermal linewidth. It is allowed within 50% deviation from fitting ^{13}CO.
3. Kinematic temperature, which is derived from ^{12}CO and is kept as a constant during fitting.
4. Optical depth. This is a relative free parameter without priori information. Initial value of 0.1 with limitation of [0, 10] is adopted during fitting.

Since the width of HINSA is narrow, a HINSA feature would become apparent in the second derivative of observed spectrum (Kavars et al. 2005). The minimization of the integrated squared sum of the second derivative would be sufficient to remove HINSA feature (Krčo et al. 2008). We follow Krčo et al. (2008) to derive $T_{\rm HI}$ by fitting a least minimum of second derivation of the input spectrum. This method performs perfectly for simple spectra but may lead to large deviation for complex spectra. The above constraints of inputting parameters are introduced to reduce uncertainty during fitting. An example of HINSA fitting is shown in Figure 3. Corresponding second derivatives of $T_{\rm HI}$ and $T_{\rm b}$ profile is shown in Figure 4. It is clearly seen that second derivatives at central velocity becomes flat. Column density of HINSA is calculated by (Li & Goldsmith 2003):

$$N({\rm HINSA}) = 1.95 \times 10^{18} \tau_0 T_{\rm x} \Delta V \ {\rm cm}^{-2}, \quad (4)$$

where τ_0, $T_{\rm x}$ and ΔV are peak optical depth, excitation temperature, and width of HINSA, respectively. The uncertainty of $N({\rm HINSA})$ is estimated through uncertainty propagation during fitting τ_0, $T_{\rm k}$ and ΔV.

3.3 Total Column Density of Hydrogen

We obtained total column density of molecular hydrogen $N_{\rm H_2}$ and its uncertainty from Planck Collaboration et al. (2016). $N_{\rm H_2}$ toward each PGCCs is derived from color extinction $E(B-V)$, which is based on multi-band continuum emission. The obtained value of $N_{\rm H_2}$ consists contribution from all gas components along line of sight of PGCCs. For PGCCs with two or more components, we assume $N_{\rm H_2}$ of each component is linearly correlated with its column density of ^{13}CO. The column density of hydrogen of each component is then calculated with

$$N_{\rm H} = N({\rm HINSA}) + 2N_{\rm H_2}. \quad (5)$$

No estimates of $N_{\rm H_2}$ are given toward PGCCs G089.62+02.16 and G093.16+09.61. $N_{\rm H_2}$ of gas components in these two sources are calculated from N(^{13}CO). Thus we have

$$N_{\rm H} = N({\rm HINSA}) + \frac{2N(^{13}{\rm CO})}{X_{^{13}{\rm CO/H_2}}} \quad (6)$$

$$= N({\rm HINSA}) + \frac{2N(^{13}{\rm CO})}{X_{^{13}{\rm C}/^{12}{\rm C}} X_{^{12}{\rm CO/H_2}}}, \quad (7)$$

where $X_{^{13}{\rm CO/H_2}}$ is ^{13}CO/H$_2$ ratio in a cloud. It contains two parts, $X_{^{13}{\rm C}/^{12}{\rm C}}$ and $X_{^{12}{\rm CO/H_2}}$. They are ^{13}C/^{12}C and ^{12}CO/H$_2$ ratio, respectively. In previous research, the value of these two parts are generally adopted as 1/60 and 1×10^4 in Galactic ISM (e.g., Liu et al. 2016).

We compare the validity of calculating $N({\rm H_2})$ by adopting $X_{^{13}{\rm CO/H_2}} = 1.67 \times 10^{-6}$ for observed PGCCs with $N({\rm H_2})$ estimation from dust. As shown in Figure 5, the adoption of $X_{^{13}{\rm CO/H_2}} = 1.67 \times 10^{-6}$ would overestimate $N_{\rm H_2}$ by a factor of 6.2. This discrepancy may originate from variation of ^{12}C and ^{13}C in ISM with different environment. We adopt $X_{^{13}{\rm CO/H_2}} = (1.05 \pm 0.36) \times 10^{-5}$ for calculating $N_{\rm H}$ in PGCCs G089.62+02.16 and G093.16+09.61.

4 RESULTS AND DISCUSSION

A total of 17 PGCCs inside FAST sky coverage were surveyed. We have detected 13 HINSA components toward 10 PGCCs, implying a HINSA detection rate of $\sim$58% in PGCCs. This detection percentage is smaller than that

of 77% in Taurus/Perseus region (Li & Goldsmith 2003, hereafter LG03) and 80% of 48 molecular clouds (Krčo & Goldsmith 2010, hereafter KG10). This deviation may arise from limited sample number and different strategy of sample selection.

We unbiasedly selected PGCCs without constraint on visual extinction and presence of Young Stellar Objects (YSOs), which could prevent cold gas from external and internal heating. An embedded YSO is found to be located inside PGCCs G108.84–00.81. Though LG03 stated that the presence of YSOs would not significantly affect the detection rate of HINSA, the statement should be checked further by including molecular clouds with far distance. In KG10, they selected sample clouds with peak visual extinction $A_{\rm V} > 6$ mag and without YSOs inside.

The spectra of sources with HINSA detection and without HINSA detection are shown in Appendix A and Appendix B, respectively. There are many reasons that may be responsible for non-HINSA detection. For example, the excitation temperature of the HI gas inside a molecular cloud is comparable to that of background continuum temperature. As shown in Figure 1, there is no obvious spatial difference between HINSA and non-HINSA detection. The sample of 17 PGGCs is small. More samples are needed to further investigate this point.

The derived parameters of CO and HINSA of all sources are shown in Table 1.

4.1 HINSA Column Density and Abundance

N(HINSA) of PGCCs has an average of 6.3$\times$ 10^{18} cm^{-2}. As a comparison, average value of $N(\rm HINSA)$ in LG03 and KG10 are 7.2$\times10^{18}$ and 6.3$\times10^{18}$ cm^{-2}. These results are consistent though we focus on a different category of molecular cloud.

HINSA abundance, $N(\rm HINSA)/N_{\rm H}$ represents abundance of cold HI in a cloud. The average HINSA abundance in PGCCs is 4.4×10^{-3}, which is about 3 times the value derived in both LG03 and KG10. We notice that $N_{\rm H_2}$ is derived from Planck data with 5′ FWHM, which is larger than that of HI (2.9′) and CO (1′) data we used. This would lead to overestimation of $N(\rm HINSA)/N_{\rm H}$. As an estimation, the peak column density $N_{\rm H_2}^{\rm peak}$ of PGCC would be 1.38 times the value of $N_{\rm H_2}$ (Planck Collaboration et al. 2016). Considering this uncertainty, the lower limit of averaged $N(\rm HINSA)/N_{\rm H}$ would be 3.2×10^{-3}.

The correlation between $\log(N(\rm HINSA))$ and $\log(N(^{13}\rm CO))$ is investigated in Figure 6. An extra uncertainty of 20% is considered due to flux calibration of ^{13}CO. As described in Section 3.2, the uncertainty of fitting complex spectrum is difficult to estimate quantitatively and is not included in the error bar of $N(\rm HINSA)$ of Figure 6. The correlation can be expressed with

$$\log(N(\rm HINSA)) = a\log(N_{^{13}\rm CO}) + b, \qquad (8)$$

in which $a = 0.52 \pm 0.26$ and $b = 10 \pm 4.1$. The Pearson correlation coefficient is 0.52, indicating an intermediate correlation between HINSA and ^{13}CO.

The uncertainty of $N_{\rm H_2}$ from dust could reach 50% the value itself. It is larger than the uncertainty percent of $N(\rm HINSA)$ and $N(^{13}\rm CO)$. The uncertainties of HINSA abundance $N(\rm HINSA)/N_{\rm H}$ and total column density $N_{\rm H}$ are significant and must be included during correlation analysis. When uncertainty in both X and Y axes are considered, the correlation between $N(\rm HINSA)/N_{\rm H}$ and $N_{\rm H}$ are fitted with the following equation:

$$\log(N(\rm HINSA)/N_{\rm H}) = c\log(N_{\rm H}) + d. \qquad (9)$$

As shown in Figure 7, there is a trend that HINSA abundance decreases along increasing hydrogen column density. The fitted parameter $c = -1.1 \pm 0.32$ and $d = 21 \pm 6.7$ when all data points are included. The slope of -1.1 ± 0.32 could not exclude the possibility that linear decrease of HINSA abundance is just due to division of $N_{\rm H}$. The two components, -3.73 km s^{-1} of G093.16+09.61 and 4.54 km s^{-1} of G107.64–09.31 show significant deviation. The ^{13}CO intensity of these two components are low, which may lead to underestimation of $N(^{13}\rm CO)$, and thus underestimation of $N_{\rm H}$ with the calculation method we used in this paper. When these two components are excluded, the fitted parameters are given as $c = -2.7 \pm 1.0$ and $d = 54 \pm 22$. The slope of -2.7 ± 1.0 indicates that the decreasing trend is physically meaningful. HINSA column density will decrease in increasing $N_{\rm H}$. This result implies that cold HI would be depleted in denser molecular cloud. Since the two components with low ^{13}CO emission would affect this analysis, more HINSA samples with accurate estimation of $N_{\rm H}$ are needed to check this correlation.

4.2 Kinematic Environment

We investigated further the kinematic environment of PGCCs. Thermal and non-thermal effects (e.g., turbulence) are two main factors that lead to line broadening. Since PGCCs are cold ($\sim 5 - 25$ K), the thermal broadening width is small, ~ 0.3 km s^{-1}. Unlike the thermal effect, the non-thermal effect does not depend on kinetic temperature and particle mass. In order to check the turbulence effect on different species, we compare non-thermal width of HINSA and CO in Figure 8. We found that non-thermal width of ^{13}CO is about $0 - 0.5$ km s^{-2} larger than that of HINSA though spatial resolution of CO (~ 1 arcmin) is smaller than that of HI (~ 3 arcmin). The smoothing of CO

Table 1 Derived Parameters of Observed Sources

Source	RA(J2000)	Dec(J2000)	Comp	^{12}CO	^{13}CO			HINSA			N(H)
				$T_{\rm ex}$ (K)	$V_{\rm cen}$ (km s^{-1})	ΔV (km s^{-1})	$N_{^{13}\rm CO}$ (cm^{-2})	$V_{\rm cen}$ (km s^{-1})	ΔV (km s^{-1})	$N_{\rm HINSA}$ (cm^{-2})	(cm^{-2})
G089.29+03.99	20:50:43.20	50:25:38.7	1	15.95±0.31	–4.41±0.02	2.85±0.04	2.18±0.05	–4.70±0.02	2.48±0.12	4.0±0.5	20.15±6.32
G089.62+02.16	21:00:44.18	49:30:29.8	1	8.47±0.87	–1.39±0.44	1.85±0.17	0.28±0.04	–1.21±0.02	1.30±0.01	3.31±0.07	2.63±0.97
			2	9.08±0.86	–0.16±0.07	1.27±0.05	0.65±0.07	–0.29±0.02	1.35±0.003	16.31±0.09	6.18±2.25
G089.64-06.84	21:37:58.08	43:11:7.8	1	18.07±0.27	12.86±0.01	1.33±0.02	1.56±0.04	12.77±0.01	0.91±0.01	3.90±0.14	13.01±7.79
G089.75-02.16	21:20:11.99	46:38:41.3	1	20.99±0.39	1.86±0.02	1.73±0.03	1.88±0.05	1.79±0.01	1.48±0.01	13.88±0.14	13.61±5.73
G090.76-04.57	21:34:00.72	45:36:504	1	17.81±0.24	10.13±0.02	1.82±0.05	0.86±0.03	10.21±0.01	1.50±0.02	7.21±0.30	5.43±2.54
G092.79+09.12	20:37:48.71	56:19:27.1	1	11.8±0.5	–2.53±0.03	1.63±0.07	0.81±0.05	–2.37±0.01	1.43±0.01	14.86±0.13	14.04±2.93
G093.16+09.61	20:36:31.44	56:54:48.6	1	8.43±0.49	–3.73±0.10	1.40±0.23	0.140±0.030	–3.61±0.01	1.00±0.03	0.68±0.04	1.34±0.55
			2	9.19±0.49	–1.75±0.02	1.19±0.04	1.28±0.25	–1.68±0.01	1.21±0.01	4.81±0.06	12.23±4.88
G107.64-09.31	23:14:26.40	50:39:44.6	1	10.9±0.4	4.54±0.22	2.20±0.50	0.115±0.034	4.72±0.02	1.27±0.04	1.86±0.13	1.16±0.51
			2	16.3±0.4	6.98±0.02	1.26±0.03	1.19±0.05	6.85±0.02	0.79±0.03	1.22±0.10	12.04±4.25
G116.08-02.40	23:56:45.11	59:44:20.0	1	16.52±0.32	–0.96±0.01	1.67±0.03	1.84±0.06	–1.00±0.01	1.54±0.02	7.14±0.23	11.22±5.02
G122.01-07.47	00:45:00.02	55:23:18.6	1	17.17±0.22	–52.18±0.02	1.23±0.04	0.59±0.03	–52.21±0.02	0.87±0.04	2.7±0.3	6.42±3.10
G089.36-00.69	21:12:24.00	47:23:32.3	1	7.43±0.28	–24.01±0.07	1.85±0.17	0.155±0.020	-	-	-	2.97± 0.84
			2	17.77±0.27	2.29±0.02	2.71±0.03	3.19±0.05	-	-	-	61.23± 17.26
			3	8.89±0.28	4.94±0.41	1.93±0.56	0.052±0.020	-	-	-	1.00± 0.28
G090.76-04.57	21:34:00.72	45:36:504	2	7.31±0.25	12.64±0.06	0.47±0.14	0.028±0.011	-	-	-	0.18±0.11
G093.22-04.60	21:44:44.88	47:13:3.4	1	17.16±0.25	3.60±0.01	1.52±0.02	2.04±0.04	-	-	-	32.9± 15.8
G093.31-11.68	22:09:44.88	41:42:30.2	1	15.32±0.39	–0.35±0.02	0.83±0.05	0.305±0.028	-	-	-	5.47±1.43
G093.36-12.07	22:11:11.52	41:25:35.8	1	8.52±0.37	0.24±0.16	0.86±0.37	0.036±0.020	-	-	-	4.09± 1.84
G101.14-15.29	22:54:59.75	42:35:51.7	1	15.45±0.43	–9.59±0.01	0.97±0.03	0.98±0.05	-	-	-	18.82± 6.39
G108.84-00.81	22:58:48.72	58:56:54.6	1	22.74±0.45	–49.67±0.02	3.27±0.04	4.73±0.10	-	-	-	86.8± 64.3
G121.93-07.67	00:44:28.34	55:11:24.4	1	17.01±0.21	–52.07±0.01	1.18±0.01	1.202±0.024	-	-	-	35.8± 13.2

data to same resolution of HI is expect to result in larger linewidth of ^{13}CO, enlarging disparity between CO and HI linewidth.

In order to check if this result is due to applying constraints of non-thermal width while fitting HINSA in Section 3.2, a wider limitation was chosen. We adopted 100% deviation from fitting ^{13}CO. Variation of fitted line width under new limitation is less than 0.5% compared to old one. Limitation of line width is used for deriving local extreme solution and does not affect fitting result.

Line broadening caused by turbulence (ΔV) is found to connect with cloud size (L) through a relation, $\Delta V \sim L^q$. The value of q is 0.38 when first proposed by Larson (1981). Further observations toward giant molecular clouds indicate a value of 0.5 (e.g., Solomon et al. 1987). This relation implies that smaller regions are less turbulent. The broader line width of ^{13}CO than HINSA may indicate that HINSA lies in a smaller, interior region than ^{13}CO.

4.3 Transition between Atomic and Molecular Phase

The existence of cold HI in clumps is due to the balance between H_2 formation on dust grains and H_2 dissociation by external environment, e.g., illumination from cosmic ray. HINSA abundance can be an effective indicator of cloud evolution (Goldsmith & Li 2005). In order to compare with an analytic model, we have to identify volume density of total hydrogen. For PGCCs with both distance estimation d (including kinematic distance derived rotation curve) and cloud size in angular resolution $\Delta\theta$, the cloud size is estimated with $L = d\Delta\theta$. For other PGCCs, we adopt the fitting formula derived in Heyer & Brunt (2004), $\sigma = 0.9(L/1{\rm pc})^{0.56}$ km s^{-1} to calculate the size of PGCCs. Average density is calculated with $\bar{n}_{\rm H} = \frac{N_{\rm H}}{L}$.

We follow the analytic model in Goldsmith & Li (2005). In a cloud with HI density of $n_{\rm HI}$ and H_2 density of $n_{\rm H_2}$, its HI density fraction $x_1 = n_{\rm HI}/(n_{\rm HI}+2n_{\rm H_2})$ as a function of time t is given by

$$x_1(t) = 1 - \frac{2k'n_0}{2k'n_0 + \zeta_{\rm H_2}}[1 - \exp(\frac{-t}{\tau_{\rm HI\rightarrow H_2}})], \quad (10)$$

in which k' is the formation rate coefficient of H_2. $\zeta_{\rm H_2}$ is the ionization rate of H_2 by cosmic-ray. The value of 5.2×10^{-17} s^{-1} has been adopted (van der Tak & van Dishoeck 2000). The time constant between atomic and molecular phase $\tau_{\rm HI\rightarrow H_2} = \frac{1}{2k'n_0+\zeta_{\rm H_2}}$. By adopting $x_1 = N({\rm HINSA})/N_{\rm H}$ and $n_0 = \bar{n}_{\rm H}$, cloud age could be calculated from Equation (10).

A solution can be derived for only 5 of 13 PGCC components. Figure 9 shows the evolution age as a function of abundance of HI and total proton density. Cloud age of these five clouds lies in the range $10^{6.7}$ yr $\leqslant \tau_{\rm cloud} \leqslant 10^{7.0}$ yr. Besides, they are located in a transition phase between unstable and steady state.

Cloud has a density profile distribution with cloud radius, e.g., power law density profile (Shu 1977), which results in a denser central region. The beam size of HI ($\sim$2.9 arcmin) and CO ($\sim$1 arcmin) observations allows us to only cover the central dense region of a PGCC clump. The estimation of cloud density by simply dividing cloud

size with column density would underestimate cloud density, leading to overestimate of cloud age. As discussed in Section 4.2, we adopt peak proton density, which is 1.38 times the current value to estimate a lower limit of cloud age. Lower limits of cloud age for five PGCC components is in the range $10^{6.6}$ yr $\leqslant \tau_{\rm cloud} \leqslant 10^{6.9}$ yr. These values are about 23% smaller than that shown in Figure 9.

We are not able to find an available solution for the remaining eight components due to relatively low HI abundance under its density. A possible reason is that cloud size was overestimated, resulting in underestimation of total hydrogen density.

5 SUMMARY

In this paper, we have observed HI spectra toward 17 PGCCs with FAST. Thirteen HINSA components are found for 10 sources. The abundance of cold HI in these clouds varies from 5.1×10^{-4} to 1.3×10^{-2} with an average value of 4.4×10^{-3}.

We found that HINSA column density in PGCCs has a intermediate correlation with ^{13}CO column density at logarithmic scale. This correlation follows a relationship of $\log(N(\mathrm{HINSA})) = (0.52\pm0.26)\log(N_{^{13}\mathrm{CO}})+(10\pm4.1)$.

When all data points are included, we could not exclude the possibility that decreasing HINSA abundance ($N(\mathrm{HINSA})/N_{\rm H}$) is due to division of $N_{\rm H}$. If we only consider HINSA components with $N_{\rm H} > 5 \times 10^{20}$ cm^{-2}, decreasing HINSA abundance as a function of $N_{\rm H}$ is physically meaningful. This confirms depletion of cold HI for forming molecular gas in more massive PGCCs.

The non-thermal linewidths of 11 of 13 HINSA components are narrower than that of ^{13}CO. This result may implicate that HINSA was located in inner and smaller region than that of ^{13}CO.

We compare our results with an analytic model of cloud evolution. Five of 13 HINSA components satisfy cloud evolution at age range of $10^{6.7} - 10^{7.0}$ yr.

Due to a limited sample of this pilot survey with FAST, there still exist some uncertainties in the above results. A larger survey of HINSA features is necessary for improving these results.

Acknowledgements We are grateful to the anonymous referee for his/her constructive suggestions, which have greatly improved this paper. This work is supported by the National Key R&D Program of China (2017YFA0402600 and 2016YFA0400702), the National Natural Science Foundation of China (Grant Nos. 11988101, 11803051, 11725313 and 11721303), CAS International Partnership Program (114A11KYSB20160008), CAS "Light of West China" Program, CAS Interdisciplinary Innovation Team and Young Researcher Grant of National Astronomical Observatories, CAS. LQ is supported in part by the Youth Innovation Promotion Association of CAS (No. 2018075).

Appendix A: DETECTED HINSA TOWARD PGCCS

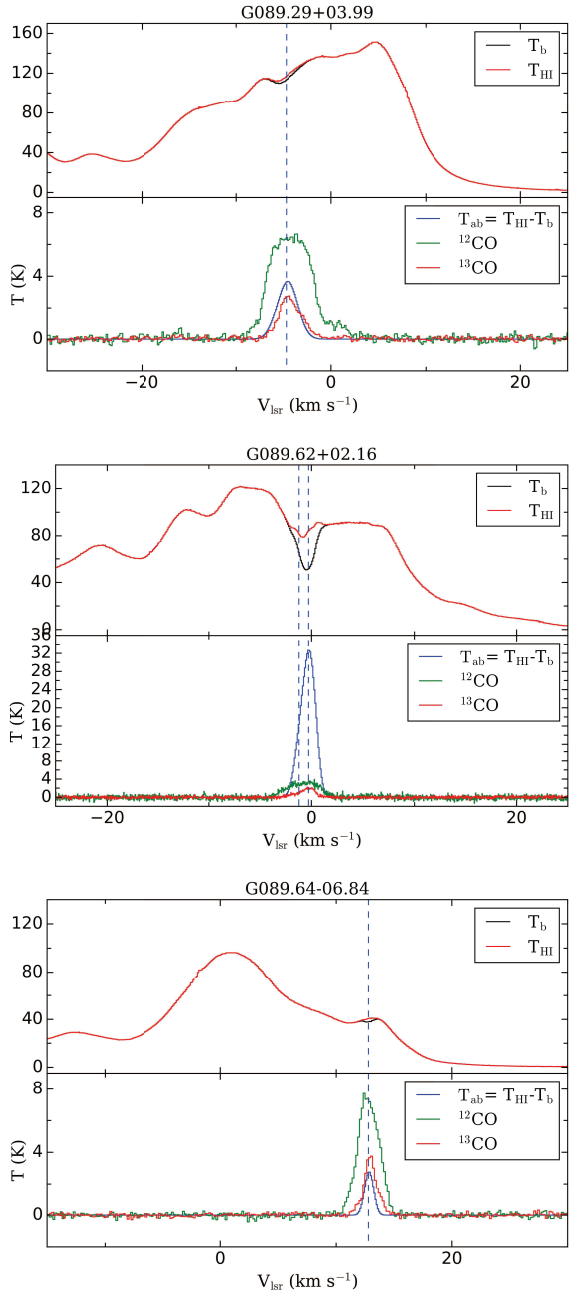

Fig. A.1 HI and CO spectra toward other nine PGCCs with HINSA . Descriptions are the same as that of Fig. 3.

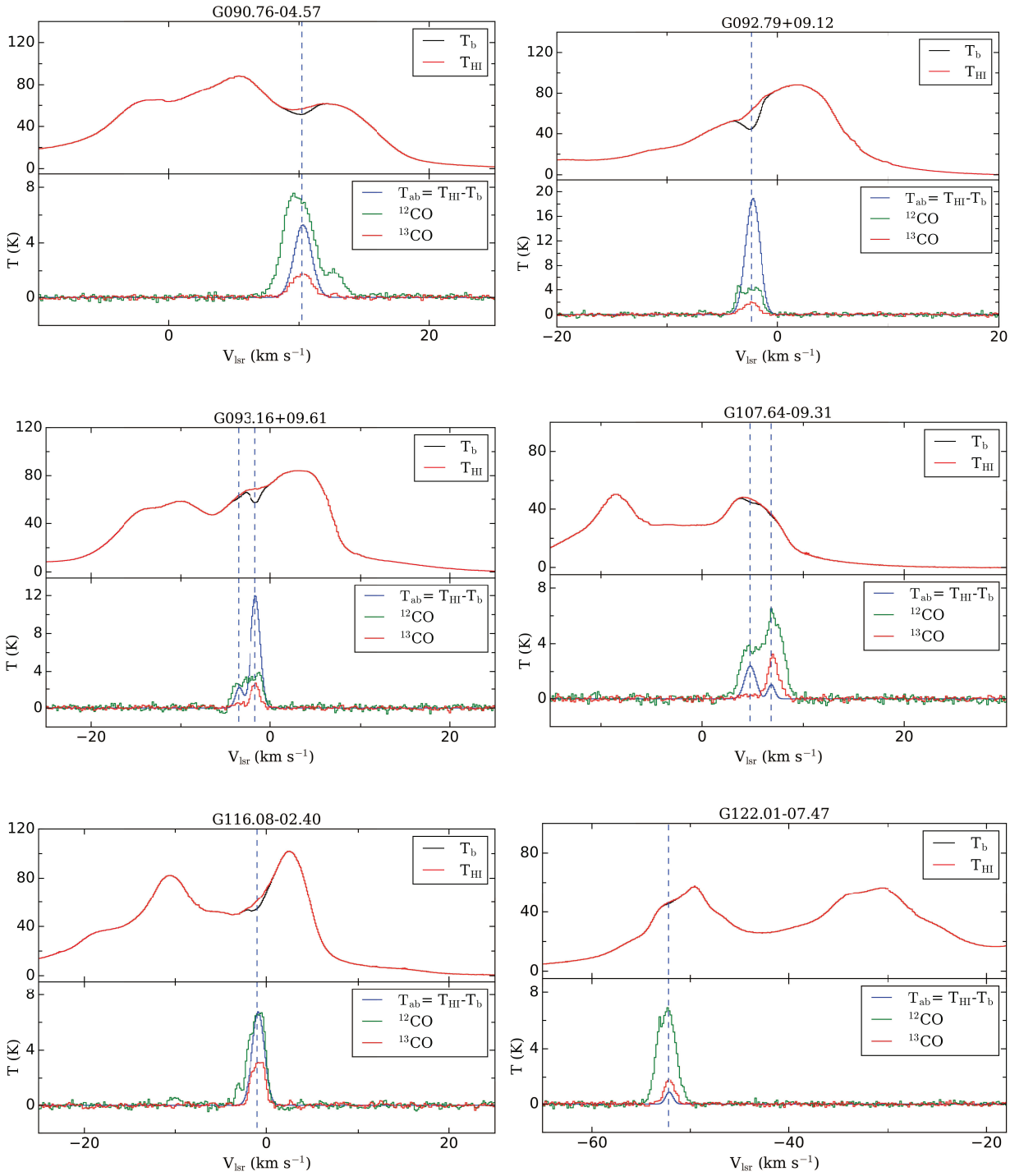

Fig. A.1 *Continued.*

Appendix B: NON-HINSA SPECTRA TOWARD PGCCS

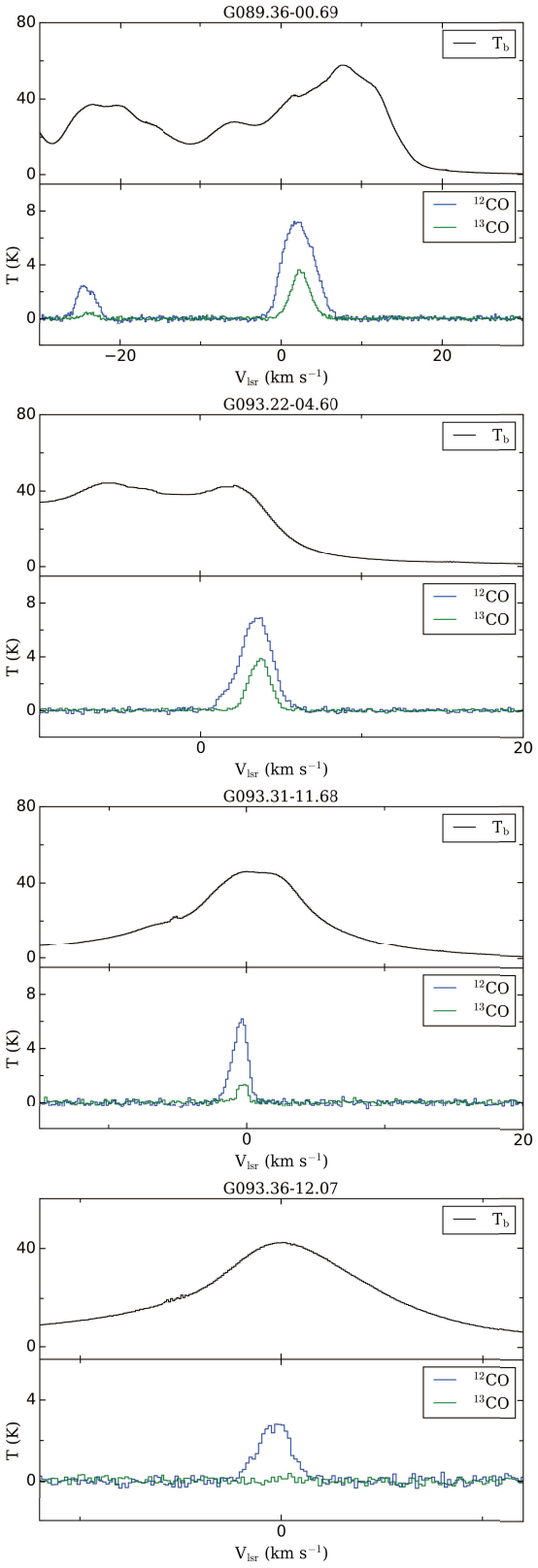

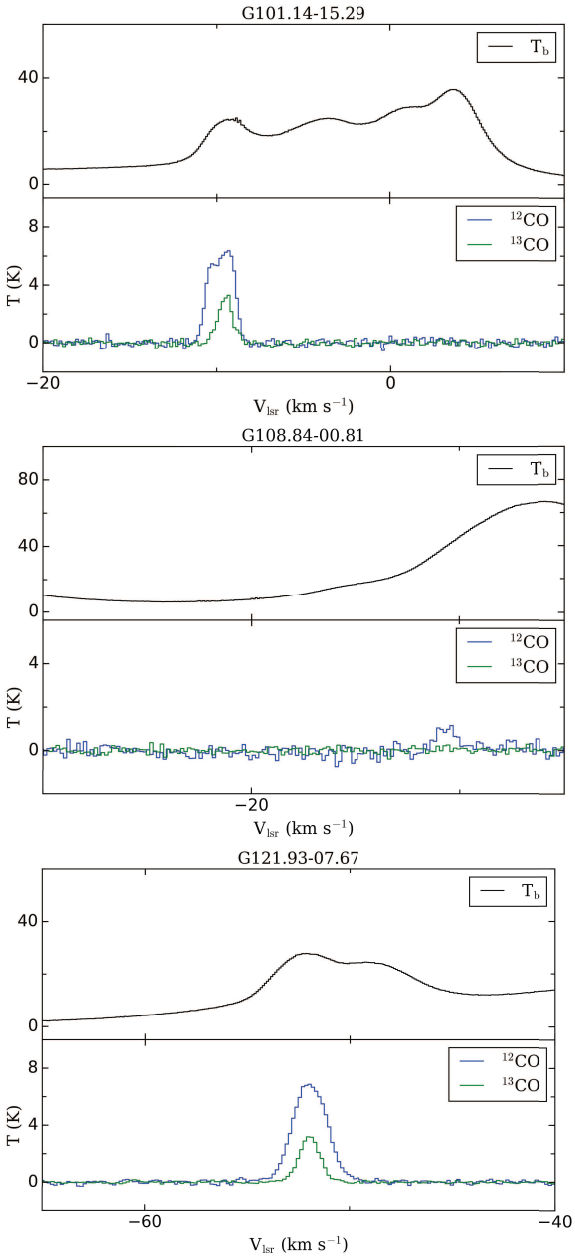

Fig. B.1 HI and CO spectra toward seven PGCCs without HINSA. The observed HI spectrum and CO spectra are shown in the top and bottom panels, respectively.

References

Brand, J., & Blitz, L. 1993, A&A, 275, 67
Dickey, J. M., McClure-Griffiths, N. M., Gaensler, B. M., & Green, A. J. 2003, ApJ, 585, 801
Gibson, S. J., Taylor, A. R., Higgs, L. A., & Dewdney, P. E. 2000, ApJ, 540, 851
Goldsmith, P. F., & Li, D. 2005, ApJ, 622, 938
Haslam, C. G. T., Salter, C. J., Stoffel, H., et al. 1982, A&AS, 47, 1
Heyer, M. H., & Brunt, C. M. 2004, ApJ, 615, L45

Jiang, P., Yue, Y., Gan, H., et al. 2019, Science China Physics, Mechanics, and Astronomy, 62, 959502
Kalberla, P. M. W., Burton, W. B., Hartmann, D., et al. 2005, A&A, 440, 775
Kavars, D. W., Dickey, J. M., McClure-Griffiths, N. M., Gaensler, B. M., & Green, A. J. 2003, ApJ, 598, 1048
Kavars, D. W., Dickey, J. M., McClure-Griffiths, N. M., et al. 2005, ApJ, 626, 887
Krčo, M., & Goldsmith, P. F. 2010, ApJ, 724, 1402
Krčo, M., Goldsmith, P. F., Brown, R. L., & Li, D. 2008, ApJ, 689, 276
Larson, R. B. 1981, MNRAS, 194, 809
Li, D. 2002, Ph.D. Thesis, Cornell University
Li, D., & Goldsmith, P. F. 2003, ApJ, 585, 823
Liu, T., Kim, K.-T., Juvela, M., et al. 2018, ApJS, 234, 28
Liu, T., Wu, Y., & Zhang, H. 2012, ApJS, 202, 4
Liu, T., Zhang, Q., Kim, K.-T., et al. 2016, ApJS, 222, 7
Liu, X.-C., Wu, Y., Zhang, C., et al. 2019, A&A, 622, A32
Lucas, R., & Liszt, H. 1998, A&A, 337, 246
Nakanishi, H., & Sofue, Y. 2003, PASJ, 55, 191
Nan, R., Li, D., Jin, C., et al. 2011, International Journal of Modern Physics D, 20, 989
Pan, Z., Li, D., Chang, Q., et al. 2017, ApJ, 836, 194
Peek, J. E. G., Babler, B. L., Zheng, Y., et al. 2018, ApJS, 234, 2
Peek, J. E. G., Heiles, C., Douglas, K. A., et al. 2011, ApJS, 194, 20
Planck Collaboration, Ade, P. A. R., Aghanim, N., et al. 2016, A&A, 594, A28
Qian, L., Li, D., & Goldsmith, P. F. 2012, ApJ, 760, 147
Shu, F. H. 1977, ApJ, 214, 488
Solomon, P. M., Rivolo, A. R., Barrett, J., & Yahil, A. 1987, ApJ, 319, 730
Solomon, P. M., & Werner, M. W. 1971, ApJ, 165, 41
Tang, N., Li, D., Heiles, C., et al. 2016, A&A, 593, A42
van der Tak, F. F. S., & van Dishoeck, E. F. 2000, A&A, 358, L79
Wu, Y., Liu, T., Meng, F., et al. 2012, ApJ, 756, 76
Yuan, J., Wu, Y., Liu, T., et al. 2016, ApJ, 820, 37
Zuo, P., Li, D., Peek, J. E. G., et al. 2018, ApJ, 867, 13